Controller Design for Propeller Phase Synchronization with Aeroacoustic Performance Metrics

Andrew Patterson*, Kasey Ackerman†, Aditya Gahlawat‡ and Naira Hovakimyan§
University of Illinois Champaign-Urbana, Champaign, IL, 61801

Noah H. Schiller¶ and Irene Gregory‖
NASA Langley Research Center, Hampton VA 23681

Active noise reduction using phase control takes advantage of the propellers used in a distributed electric air vehicle by treating each propeller as an independent acoustic source. These acoustic sources can destructively interfere if the propellers are synchronized. With this method, the radiated sound power around the vehicle can be reduced. The purpose of this paper is to design a controller that regulates propeller positions to reduce the radiated sound power through destructive interference and to demonstrate the performance of the controller through acoustic testing.

There are two control requirements for reducing the sound pressure level considered in this paper. The first is accurately regulating the difference between the propeller azimuthal blade positions (phase) relative to their neighbors. By changing the phase at the source, we can control the phase of the sound wave at an arrival position to create destructive interference. The second consideration is maintaining high coherence between the two propeller sources. To achieve significant attenuation, the controller needs to regulate phase error and suppress sources of incoherence.

Performance is demonstrated through sound recordings performed in the NASA Langley Structural Acoustic Loads and Transmission (SALT) anechoic chamber. We show that the controller is capable of reducing sound pressure level at a given observer location by 17 dB at the blade passage frequency and that this method can reduce the radiated sound power by 6 dB at the blade passage frequency.

I. Introduction

Active noise reduction through propeller phase synchronization builds upon previous research that leveraged phase synchronization to reduce vibration [1] and reduce the aircraft's internal sound pressure level [2]. Recent work extends these results to include a larger class of air vehicles and focuses on external, rather than internal, sound pressure level reduction. Since direct feedback for external sound pressure reduction is difficult to implement, accurate acoustic estimation is necessary. A framework, originally presented in Ref. [3] and inspired by Ref. [4], for using acoustic estimation to reduce sound pressure level is shown in Figure 1. As shown in this figure, the acoustic estimation method uses the vehicle dynamics to estimate the current spatial-acoustic profile of the aircraft and compare it to a desired profile. Based on the difference between the desired and estimated sound pressure levels, the acoustic controller and phase controller adjust the motor speed commands to change the phase synchronization of the propellers. This work presents acoustic results that validate the feasibility of phase control for noise reduction.

The control solution presented in this paper is designed for distributed electric propulsion air vehicles. These vehicles use electric motors rather than combustion engines to propel the aircraft and typically have propeller configurations conducive for phase synchronization. Benefits of this type of aircraft configuration can be found in Refs. [5] and [6]. There are two key advantages of this configuration for noise reduction applications. The first is the actuator dynamics. Electric motors typically have high actuation bandwidth, which allows their speed to be rapidly adjusted to achieve

---

[*] Doctoral Student, Dept. of Mechanical Science and Engineering, AIAA Member.
[†] Doctoral Student, Dept. of Mechanical Science and Engineering, AIAA Member.
[‡] Postdoctoral Research Associate, Dept. of Mechanical Science and Engineering.
[§] Professor, Dept. of Mechanical Science and Engineering, AIAA Fellow.
[¶] Research Engineer, Structural Acoustics Branch, AIAA Member.
[‖] Senior Research Engineer Dynamic Systems and Control Branch, AIAA Associate Fellow.

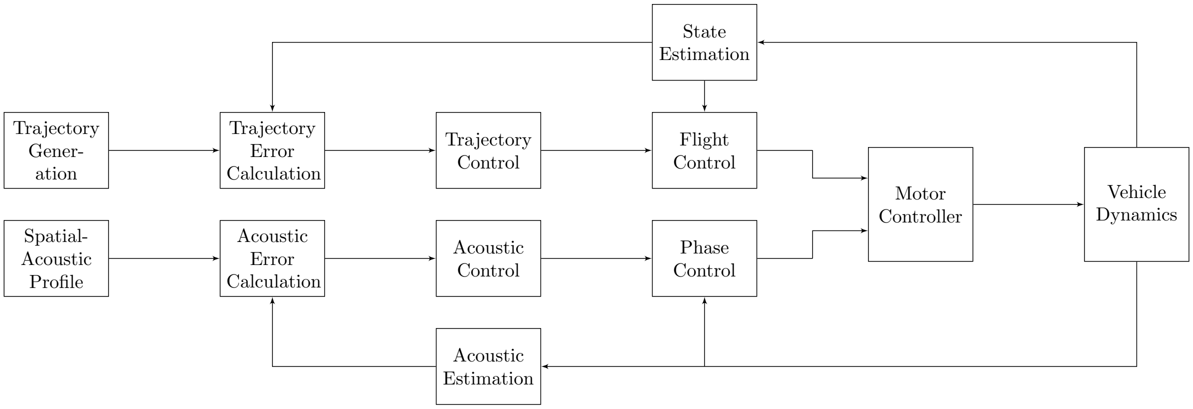

Figure 1 Acoustic control framework for unmanned systems.

synchronization requirements. The second advantage is scalable design, allowing many motors to be placed on the vehicle, for improved aerodynamic performance, control and redundancy [7]. This second benefit allows noise reduction to be attempted with a large number of actuators, all acting as controllable acoustic sources as suggested in Ref. [8].

Phase control is necessary to ensure that the sound waves generated by the propellers interfere destructively, instead of constructively, at a specific location. The phase offset of a propeller is the mean difference between the azimuthal position of the propeller relative to a reference. This reference can either be a real, neighboring propeller or a virtual propeller. In this work, the phase offset is calculated between two neighboring propellers. An example of the phase angle notation is shown in Figure 2. Adjusting the phase separation of synchronized propellers alters the spatial distribution of

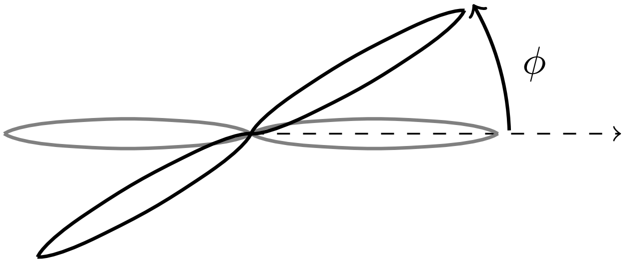

Figure 2 Propeller phase for two bladed propeller. The phase angle, ϕ, of the black propeller is measured with reference to the neighboring reference propeller, shown in gray.

the sound pressure level at the blade passage frequency. The goal of phase control is to reduce the sound pressure level in a specified region, or over the entire region, by maintaining a specified phase offset during vehicle operation.

Initial work on phase control is suggested in Ref. [8], where the potential sound reduction is simulated for a vertical takeoff and landing aircraft in forward flight. This work considers noise reduction potential in the presence of steady-state phase offset errors and added Gaussian white-noise. Based on the metrics of mean and standard deviation of phase error given in Ref. [8], an initial proof of concept is demonstrated on a testbed in Ref. [3]. On this testbed, the motor position is controlled to track a phase angle relative to the virtual propeller. The performance of the controller is compared in terms of steady-state offset and tracking error variance. While this testbed demonstrates feasibility, the controller performance is not directly related to sound pressure level reduction. In Ref. [9], an expansion of noise reduction models is presented in terms of coherence between propellers. With this relation, the controller can be directly designed to minimize sound pressure level by minimizing steady-state phase offset error and maximizing the coherence between the propellers. The motor model again includes additive Gaussian white-noise as well as a low frequency sinusoidal disturbance to motor position. Recent work that focuses not just on a single observer location but on net radiated power can be found in Ref. [10]. In addition, this work suggests that phase control can be extended to vehicles that use propeller speed adjustment for stabilization, such as an octocopter, provided there is sufficient actuator redundancy.

Based on the contributions of these papers, we present a control architecture that directly controls phase offset and is designed to minimize the steady-state phase offset error while maximizing the coherence for a two propeller system. To maximize coherence, the controller is designed to reduce the contributions of noise, disturbances and nonlinearities in the motor/propeller system.

This paper begins with an overview of the experimental setup in Section II that will be used to validate the acoustic performance of the control system. The definitions and models used in the paper are presented in Section III. In Section IV, we explain the acoustic model used for control design and for calculating expected control performance. In Section V, the methods used for phase control are presented. The controller's performance is discussed in Section VII.

II. Experimental Setup

In order to validate the aeroacoustic performance of the phase control algorithm for a distributed electric propulsion aircraft, the tests are designed with a simple, two propeller system in mind. The tests are performed in an anechoic chamber to simulate the propeller system in a free-field acoustic environment. The experimental setup is designed to be comparable to the setup found in Ref. [10], with the introduction of a software phase control system that can be continuously adjusted rather than a mechanical linkage-based phase control system.

A. Aircraft Configuration

The aircraft configuration considered in this work is a distributed electric propulsion vehicle with two synchronized propellers. Though only two propellers are synchronized in this work, the vehicle may have any number by straightforward extension of the methods presented. The key assumption is that the propellers are driven by electric motors capable of high bandwidth speed control. It is assumed that these motors will be brushless DC motors, with associated electronic speed controllers (ESCs) to convert throttle commands into the necessary voltage waveforms for actuation. While sufficient for many applications, ESCs typically do not measure motor angular position. To address this deficiency, a sensor is needed for continuous position feedback. Therefore, the three components of the aircraft included on the testbed are the motors, ESCs and position sensors.

B. Testbed

To meet these design requirements, the testbed assembly is constructed as shown in Figure 3. The testbed uses two corotating propellers that have two blades each. Both propellers are driven by independent brushless DC motors, controlled by MT40A-OPTO ESCs. These components are commercial off-the-shelf components designed for hobbyist use. The position feedback is provided by an RLS AM4096 magnetic position encoder, which outputs a 10-bit analog voltage representing the wrapped position of the motor. The magnet for the encoder is mounted on the rear output-shaft of the motor.

The propellers each have a diameter of 317 mm and their centers are separated by 400 mm. The rotation rate target speeds of the motors are set to 4,500 RPM, unless otherwise specified. This constant speed corresponds to the nominal flight condition of the notional aircraft configuration where stabilization and maneuvering can be achieved, without changing motor speed, by using other actuators such as aerodynamic surfaces. Note that a motor rotation rate of 4,500 RPM is equal to 75 Hz. Therefore, for a two-bladed propeller, the blade passage frequency is 150 Hz.

The motor speed commands and the position feedback are controlled using a SpeedGoat IO104 data acquisition module running at 9600 Hz with Simulink® Real-Time software. The speed and phase controllers are artificially limited to sending throttle commands every 100 Hz.

C. SALT Chamber

The propeller rotor assembly is installed in the center of the NASA Langley Structural Acoustic Loads and Transmission (SALT) anechoic facility. The surfaces of the chamber are covered with acoustic wedges and the dimensions are 9.63 m by 7.65 m by 4.57 m measured from wedge tip to wedge tip. The testbed is mounted vertically, as shown in Figure 3, to reduce structural load during testing. The anechoic chamber creates a near free-field acoustic environment and contains five free-field microphones located at a distance of 1.9 m from the center of the testbed. The elevation angles of the microphones are 0°, -11.25°, -22.5°, -33.75° and -45°, where the negative sign indicates that the microphones are located below the plane of the propellers. These microphones are denoted M1-M5, with M1 being mounted at 0° elevation. The microphones are all located at the same azimuthal angle.

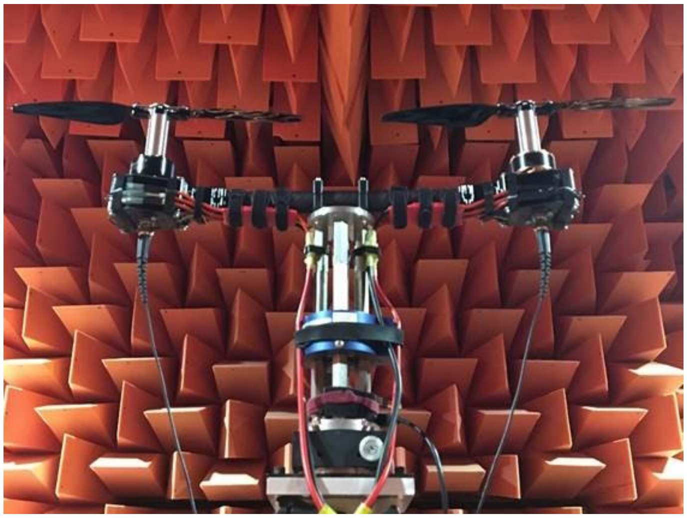

Figure 3 Testbed in the SALT facility.

While this chamber does not simulate the aerodynamic environment of an aircraft, flow recirculation does occur in the closed chamber, which introduces mild perturbations to the system. Rejection of this aerodynamic disturbance is of interest for control design. Though phase control may affect harmonics past the blade passage frequency, recirculation in the chamber can reduce the consistency of the sound measurements at higher harmonics. Therefore, only the measurements at the blade passage frequency are considered.

The five free-field microphones are simultaneously sampled at 51.2 kHz via National Instruments™ data acquisition hardware controlled with MATLAB®. A single recording session involves bringing the motors up to speed and regulating the phase offset while recording. To measure radiated sound power, multiple recording sessions are conducted, with the set of five microphones in a different azimuthal angle for each recording session.

III. Modeling

The basis of phase control can be found in both Refs. [4] and [9]. The key observation is that each propeller contributes to the sound pressure linearly. Phase control attempts to control the propeller angular positions to achieve destructive interference at specified observer locations. We formalize these terms with the following definitions.

A. Motor and Propeller Model

The motor dynamics are described by a second order state-space model. The motor model is found in Ref. [3] and given by the following equation:

$$\begin{aligned}
&\dot{x}(t) = Ax(t) + Bu(t), \quad x(0) = x_0\\
&y(t) = Cx(t),\\
&A = \begin{bmatrix} a_{11} & a_{12} & 0 \\ a_{21} & a_{22} & 0 \\ 0 & 1 & 0 \end{bmatrix}, \quad B = \begin{bmatrix} b_1 \\ 0 \\ 0 \end{bmatrix}, \quad C = \begin{bmatrix} 0 & 0 & 1 \end{bmatrix}, \quad x = \begin{bmatrix} I \\ \omega \\ \theta \end{bmatrix} \quad \text{and} \quad x(0) = x_0.
\end{aligned} \tag{1}$$

The state includes the motor current, I, motor angular velocity, ω, and motor position θ. The parameters of A and B vary depending on the chosen motor propeller combination. The phase controller reference command is either a reference motor velocity, $r_\omega(t)$, or a reference phase, $r_\phi(t)$. Since the testbed is composed of two motors, we use a superscript on the state equations and variables to indicate the motor to which the variables correspond. For example, the first motor's position is θ^1, while the second motor position is θ^2. When the superscript is neglected, the equation could refer to either motor.

The state-space model reflects that only position is measured. The measured position is denoted $\hat{\theta}(t)$ and is modeled as a function of the true position:

$$\hat{\theta} = \mod(\theta + \delta(t) + \gamma(t), 2\pi) + \nu(t),$$

where $\delta(t)$ is a disturbance, $\gamma(t)$ is sensor nonlinearity and $\nu(t)$ is measurement noise. The disturbance is assumed to be low-frequency and semiperiodic, representing the aerodynamic effects on the motor position. The sensor nonlinearity is periodic with the same frequency as the motor rotation rate, representing sensor alignment errors.

B. Propeller Contribution Model

The contribution of each propeller to the sound pressure level, at observer m, is described in detail by the authors of Ref. [9]. We will consider a simplified version for use in control design that combines the pressure amplitude, distance and source radius into a single constant, c_{n,m,n_h}. The number of blades and number of propellers are assumed to be constants. Therefore, the contribution for each propeller at observer m is given by the definition:

$$p_m(t) = \sum_{n=1}^{2} \sum_{n_h=1}^{N_H} c_{n,m,n_h} \sin(\theta^n(t)), \tag{2}$$

where n indicates the propeller number, n_h indicates the harmonic number of the blade passage frequency, N_H is the highest harmonic considered, t is time and $\theta^n(t)$ is the angular position of the n^{th} propeller. In this work, $N_h = 1$.

IV. Aeroacoustic Performance

The acoustic performance of the phase controller is modeled in Equation 2. As shown in Ref. [10], both the sound pressure level in a specific direction and the total radiated sound power can be altered by adjusting the relative phase offset between the two propellers. These results specifically address sound pressure level and radiated sound power at the first harmonic of the blade passage frequency.

A. Sound Pressure Level

Changing the phase angle between the two propellers results in different sound pressure levels in every direction around the source propellers. This phase adjustment changes the shape and direction of the acoustic radiation pattern. The shape of the acoustic radiation may be anything from a circular radiation pattern to a cardioid to a complex multilobed pattern. Fully characterizing this radiation pattern in the SALT anechoic chamber requires multiple acquisitions, with the microphone array positioned at various azimuthal angles around the propeller. Unfortunately, this characterization removes the ability to compare controller performance to acoustic performance at specific time instances, since each acquisition is performed with a different test.

To compare the controller performance and acoustic performance in real time, the sound pressure level will be considered for only a single microphone array position. The microphone array azimuth angle is locked at 0°. At this angle, all five microphones record but only the sound pressure level recorded by microphone M1, at an elevation of 0°, is presented in this work.

At this microphone position, and with a propeller phase separation of 90°, the microphone is ideally expected to measure zero sound pressure level at the blade passage frequency. Realistically, the measurement will not approach the theoretical limit. The sound pressure level is given in units of dB relative to 20×10^{-6} Pa. Equation 4 in Ref. [9], provides an estimate of the sound pressure level reduction, in dB, for a given coherence:

$$\Delta = 10 \log_{10} [1 - |\gamma(f)|], \tag{3}$$

where $|\gamma(f)|$ is the magnitude of the complex coherence between the two propeller positions at a frequency, f.

B. Radiated Sound Power

The total radiated sound power provides an acoustic metric that is not limited to a specific direction. Setting the phase angle between the two propellers to 90° reduces the radiated sound power at the blade passage frequency. The radiated sound power is calculated based on many sound pressure measurements collected around the propeller assembly. Details of this power calculation can be found in Ref. [10]. The radiated sound power is given in units of dB relative to the baseline radiated sound power of two unsynchronized propellers. For a 90° phase separation, the ideal reduction in radiated sound power at the blade passage frequency is 6.2 dB for two propellers at 4500 RPM with a hub to hub separation distance of 0.4 m.

The method of computing the radiated sound power requires a test to be run multiple times at different microphone array azimuth angles. This procedure precludes the direct comparison of the controller's performance at any specific time to the radiated sound power at that same time, since it is computed using multiple tests.

V. Methods

A. Angular Difference

Rotation matrices are used to represent the rotation of the motors. A rotation around a single axis by an angle θ can be represented by the two dimensional rotation matrix:

$$R(\theta) = \begin{bmatrix} \cos\theta & -\sin\theta \\ \sin\theta & \cos\theta \end{bmatrix}.$$

Given a rotation matrix, the angle (with range $-\pi$ to π) can be recovered using the arc-tangent function:

$$\theta = \operatorname{atan2}(\sin\theta, \cos\theta).$$

The rotation matrix difference between two angles, θ_1 and θ_2, is given by the equation

$$R(E(\theta_1, \theta_2)) = R(\theta_1) R(\theta_2)^\top,$$

where $R(\theta)^\top$ is the matrix transpose. After computing the rotation matrix difference, $R(E(\theta_1, \theta_2))$, the difference in rotation can be recovered by using the arc-tangent function:

$$E(\theta_1, \theta_2) = \operatorname{atan2}(r_{21}, r_{11}), \tag{4}$$

where r_{xy} is the element in the x^{th} column and y^{th} row of $R(E(\theta_1, \theta_2))$.

B. Speed Calculation

The speed estimate is calculated using the difference between measured positions at each time step. Since the measured position is a wrapped value, the speed cannot be calculated directly using a finite difference method, but requires a nonlinear transformation such as unwrapping. The unwrapped difference is represented with the function E, defined in Section V.A. The speed, $\hat{\omega}(t)$, is calculated using a finite difference method, given by the equation:

$$\hat{\omega} = E(\hat{\theta}_n, \hat{\theta}_{n-1}) \cdot \frac{1}{\mathrm{h}},$$

where h is the sampling period, $\hat{\theta}_n$ is the current position estimate, and $\hat{\theta}_{n-1}$ is the previous position estimate.

The speed error calculation is defined by the equation:

$$e_\omega = r_\omega - \hat{\omega},$$

where r_ω is the desired operating speed.

C. Phase Calculation

The phase difference is calculated between the motor position and the reference motor position. Unlike the true position, the measurement is wrapped to a range of width 2π. The nonlinear difference, E, is used to determine how the two wrapped position signals compare. Letting motor one be the reference motor, the phase difference calculation becomes

$$\hat{\phi} = E(\hat{\theta}^1, \hat{\theta}^2),$$

where $\hat{\theta}^1$ is the measured position of the first motor, and $\hat{\theta}^2$ is the measured position of the second motor. Given the phase offset estimate, the phase error calculation is defined by the equation:

$$e_\phi = r_\phi - \hat{\phi}.$$

D. Filtering

The motor position is an analog signal subject to measurement noise. In order to reduce the effects of this noise, the sensor measurement is filtered using a second-order Butterworth filter, with a cutoff frequency of 16 Hz. This bandwidth is chosen to reduce high frequency measurement noise without filtering out the dominant dynamics of the motor. A similar filter is used for filtering the speed estimate produced by the finite difference method. This filter bandwidth is chosen to reduce the effect of the sensor nonlinearity, which introduces a periodic measurement error at the motor rotation rate of 75 Hz. The filter cutoff frequency of 16 Hz attenuates the periodic sensor nonlinearity by 26 dB.

Ideally, these filters would be implemented using a nonlinear filter that uses knowledge of the rotation structure used to calculate angular differences. For example, a first-order lowpass filter can be designed using a technique called spherical linear interpolation [11]. However, the noise added after the rotation operation has already occurred is significant, therefore, the measured angle is not strictly limited to the range $[0, 2\pi)$. For this reason, linear filtering of the rotation matrices is used in the implementation of these position and speed filters. The linear filtering method applies identical second-order Butterworth filters to each element of the rotation matrix, before Equation 4 is used to recover the angle. This operation does not directly operate on the rotation matrix structure, and so the filtered rotation matrix will not be a well defined rotation matrix. To recapture the rotation matrix structure, the filtered matrix may be orthonormalized.

E. Speed Control

The speed controller is expected to have reached steady-state before phase synchronization begins. For the purpose of speed control in this paper, the speed controller is chosen to be a proportional-integral controller. After the phase controller is enabled, the speed controller of the second motor latches its output and cedes control to the phase controller, as described in section V.F. The controller is described by the equation:

$$u_\omega(t) = k_{p,\omega} \cdot e_\omega(t) + k_{i,\omega} \int_{t_0}^{t} e_\omega(\tau)\mathrm{d}\tau,$$

where u_ω is the motor speed command generated by the speed controller, $k_{p,\omega}$ is the proportional gain, $k_{i,\omega}$ is the integral gain, t_0 is the time at which the speed controller is enabled, and t is the current time.

F. Phase Control

The phase controller is chosen to provide zero steady-state error using a proportional-integral-derivative (PID) controller. The controller is ideally described by the equation:

$$u_\phi(t) = k_{p,\phi} e_\phi(t) + k_{i,\phi} \int_{t_0}^{t} e_\phi(\tau)\mathrm{d}\tau + k_{d,\phi} \frac{\mathrm{d}e_\phi(t)}{\mathrm{d}t},$$

where u_ϕ is the motor speed command generated by the phase controller, $k_{p,\phi}$ is the proportional gain, $k_{i,\phi}$ is the integral gain, $k_{d,\phi}$ is the derivative gain, t_0 is the time at which the phase controller is enabled, and t is the current time. The derivative term is not realizable and so the implementation involves a first-order filtered finite difference approximation of the error derivative. The cutoff frequency of the filter is set to NT_s where T_s is the sampling period of the controller and N is a tuneable constant, chosen to be 10 in this case.

A robust phase controller is designed around the linear motor model, with a large phase margin and low bandwidth. The robust controller has a phase margin of 70° and a bandwidth of 1 Hz. This margin reduces the overshoot due to large step changes in phase, and increases robustness to model uncertainty. However, the low bandwidth does not allow the controller to sufficiently reject the recirculation disturbance.

An aggressive phase controller is designed around the linear model, with a smaller phase margin and a slightly extended bandwidth. The aggressive controller has a phase margin of 25° and a bandwidth of 2 Hz, which is sufficient for rejecting the recirculation disturbances.

G. Control Logic

In order to prevent conflict between speed and phase control objectives on the control channel, u, the following control logic is proposed. Motor one, with control input $u^1(t)$, acts as the reference motor and does not contribute to regulating the motor phase. Therefore, the control input is only affected by the speed controller:

$$u^1(t) = u_\omega^1(t),$$

for the entire test duration, where u_ω^1 is the speed controller output for motor one.

The second motor attempts to follow the reference motor, motor one, with a phase offset. To achieve this goal, the control input $u^2(t)$ is defined in the following way:

$$u^2(t) = \begin{cases} u_\omega^2(t) & t < T_\phi, \\ u_\omega^2(T_\phi) + u_{\phi,r}(t) & t \geq T_\phi, |e_\phi| > \frac{\pi}{5} \\ u_\omega^2(T_\phi) + u_{\phi,a}(t) & t \geq T_\phi, |e_\phi| \leq \frac{\pi}{5} \end{cases},$$

where T_ϕ is the time that the phase controller is activated, $u_{\phi,r}(t)$ is the robust phase controller and $u_{\phi,a}(t)$ is the aggressive phase controller. Notice that the speed command u_ω^2 is locked to the value at the time of the phase controller's activation. The controller cases are referred to as cases 1, 2 and 3, sequentially.

VI. Results

The results of the acoustic tests are demonstrated for three cases: uncontrolled phase, robust phase control, and aggressive phase control. For each of these cases, the controller performance is shown in terms of the motor phase error, shown in Figure 4. A detailed view of the sound pressure level at the blade passage frequency over time is also provided in Figure 5. The overall performance during the time interval is given in terms of the short-time Fourier transform calculated with a Hanning window, 90% overlap, and a frequency resolution of 5 Hz, as shown in Figure 6. The joint time-frequency acoustic performance is shown as a spectrogram of the sound pressure level in Figure 9 of the appendix.

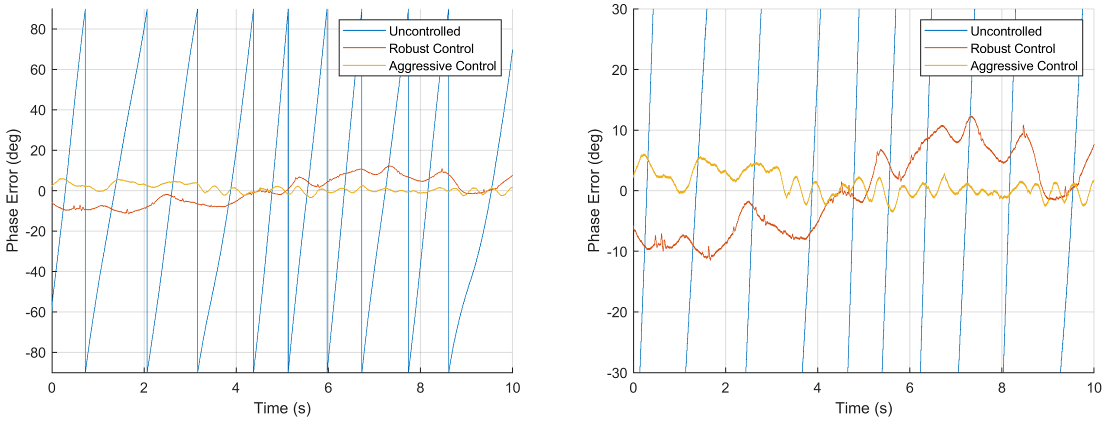

(a) Phase error over full output range.

(b) Phase error over time .

Figure 4 Phase error over time for three different 10 second tests.

A. Uncontrolled Response

The uncontrolled performance is demonstrated by fixing the throttle commands of the two speed controllers with a slight, 0.2%, difference between their values. This results in a 20-40 RPM speed difference, which causes the propeller phase offset error to drift as shown in Figure 4a. Note that since the propellers have two nominally identical blades each, the phase error has been wrapped to the range $-90°$ to $90°$. In Figure 5, we see that the phase drift can be directly related to the sound pressure level at the blade passage frequency. The sound pressure level oscillates between 40 and 60 dB. The troughs of the sound pressure level, seen in Figure 5, correspond to the phase angle passing through 0° phase error in Figure 4, which corresponds to a phase offset of 90°. Figure 6 shows the power spectra over the entire test interval, computed using a fast Fourier transform with a Hanning window, 90% overlap, and a frequency resolution of 5 Hz. We see that the first harmonic of the blade passage frequency (150 Hz) has an amplitude of approximately 57 dB.

B. Robust Controller Performance

The robust controller is designed to operate at 4,500 RPM and be able to accurately track any phase offset target. However, to achieve this full range of control, the controller is not aggressively tuned. The propeller phase error achieved

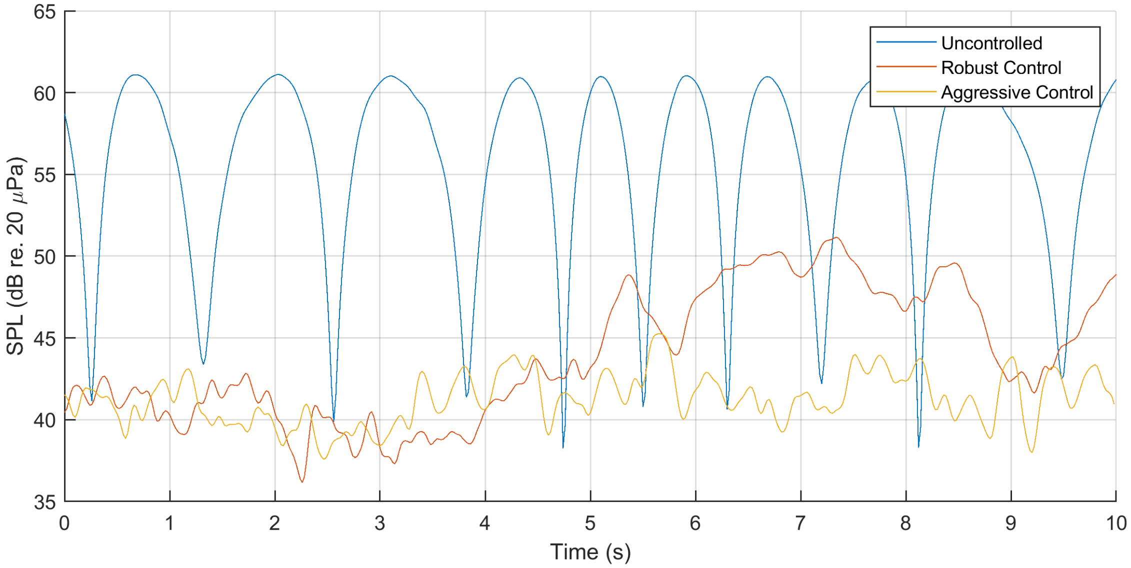

Figure 5 Sound pressure level at the blade passage frequency over time.

by this controller is shown in Figure 4. The propeller phase is centered around 0° error but drifts by over 10°, with large deviations at 1.5 and 7.25 s. In this case, the controller has some ability to reject disturbances and maintain the target phase offset. The resulting sound pressure level at the blade passage frequency is shown in Figure 5, and the measured sound pressure level reduction at the blade passage frequency can be observed as a function of time. The sound pressure level drifts between 40 and 50 dB as the phase error drifts away from 0° at approximately 7.25 s. In the sound pressure level calculated over the entire time interval, we see that the robust controller produces a significant sound pressure level reduction, 11 dB, at 150 Hz.

The radiated sound power was measured using this controller. The radiated sound power measurement required many different acquisitions with the microphone array moved relative to the motor assembly for each acquisition. As a result, the acoustic performance of this metric cannot be related to the time history of the controller's performance metrics. Furthermore, since the radiated sound power is less sensitive to small phase errors, the robust controller's performance is sufficient to provide a significant reduction. The calculated radiated sound power during phase control with the robust controller is -6 dB relative to the radiated sound power calculated for unsynchronized propellers.

C. Aggressive Controller Performance

The aggressive controller operates in a small region around zero phase error. The limited region of operation allows the controller to be aggressively tuned. The resulting controller performance is shown in Figure 4. The phase drifts due to disturbances only half as much as the robust controller, with a maximum deviation of approximately 5°. The acoustic performance reflects the higher control accuracy, shown in Figures 5 and 6. In Figure 5, the average sound pressure level at the blade passage frequency is around 40 dB, with a maximum value of 45 db. The average sound pressure level over the entire interval, shown in Figure 6, shows an additional reduction of 5 dB to a total reduction of 17 dB in sound pressure level at the blade passage frequency when compared to the baseline unsynchronized case.

D. Speed Change

In addition to steady-state phase control, we demonstrate two speed changes of 100 RPM while the aggressive controller attempts to maintain zero phase error. The speed changes are realized as step reference changes for motor one while motor two's controller continues to attempt phase control with the aggressive controller, $u^2(t) = u^2_\omega(T_\phi) + u_{\phi,a}(t)$. These steps are known a priori but the knowledge is not used to increase tracking performance. The phase error is shown in Figure 7. The controller performance is similar to the performance in steady-state, with larger errors during transition. The spectrogram of the microphone response to the step change is shown in Figure 8. The spectrogram shows that the acoustic performance is similar to the steady-state performance outside the transition period, which is

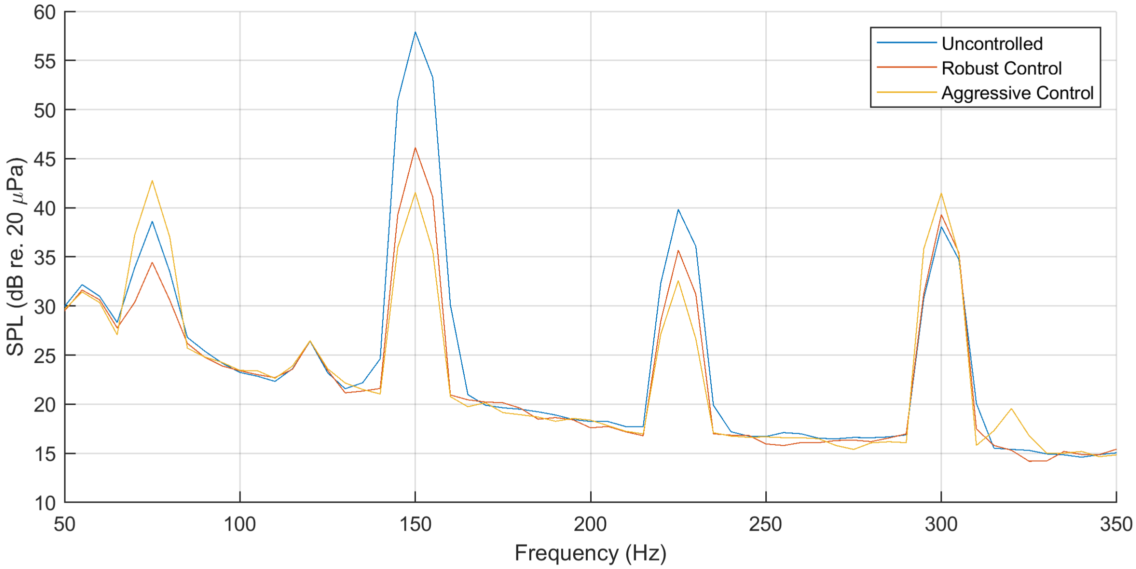

Figure 6 Sound pressure level at the blade passage frequency over the frequency range of interest.

dominated by steady-state phase error. The phase error could be further reduced using a feasible speed transition and feedforward derivative term as performed in Ref. [3] for phase transition.

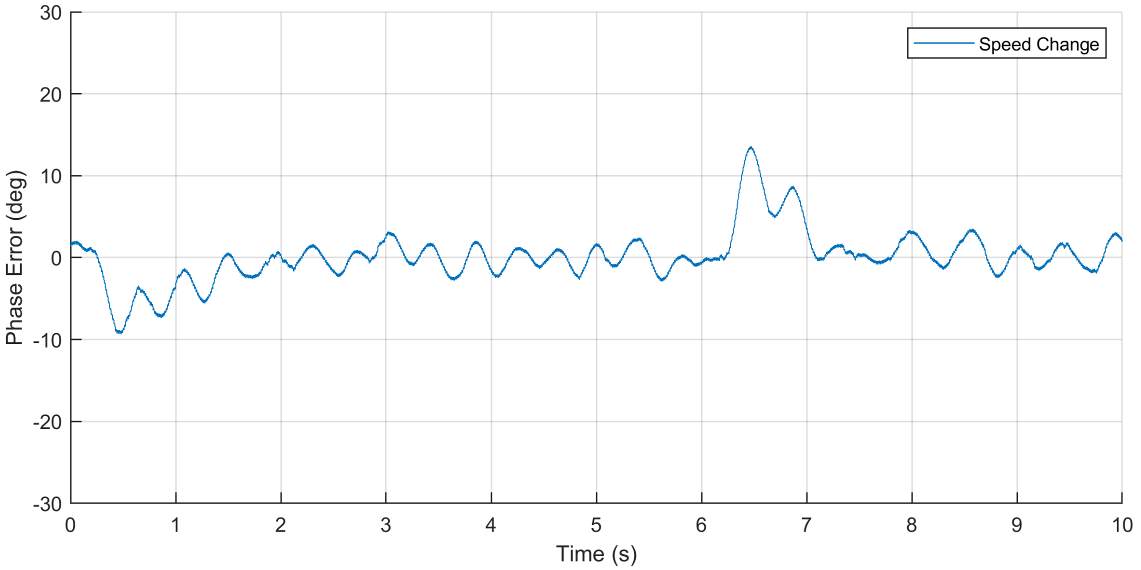

Figure 7 Phase error during speed changes. Speed changes occur at 0 s and 6 s.

VII. Conclusion

This paper presents a control architecture that directly controls the phase difference between propeller blades. This controller is designed and demonstrated for a two propeller system. The controller performance is quantified in the time domain, with phase error calculated at each time step. The designed controller is demonstrated to achieve the necessary stability and steady-state performance. The transient performance is also demonstrated for small speed reference changes.

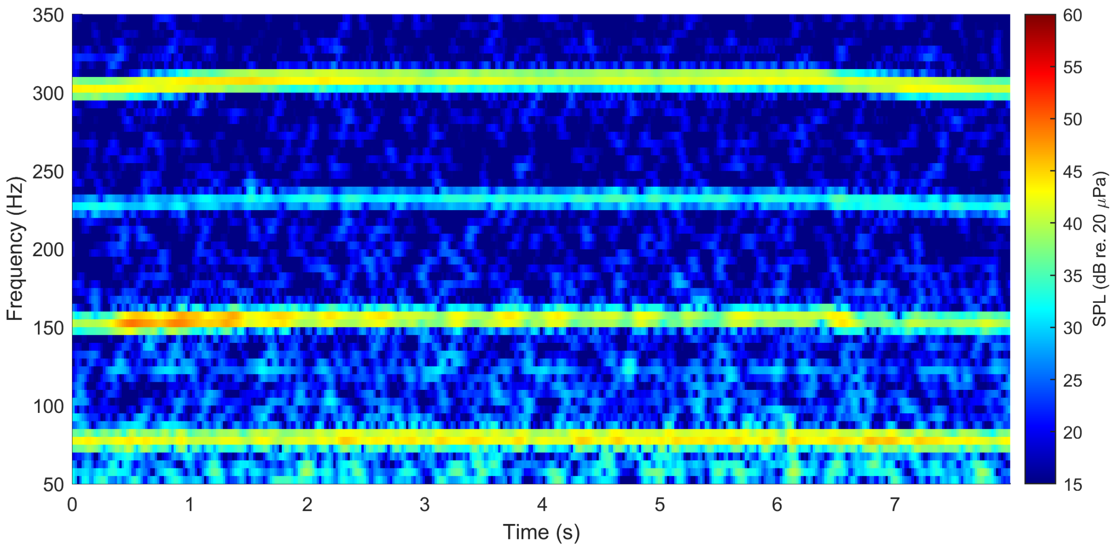

Figure 8 Spectrogram during speed change. Speed changes occur at 0 s and 6 s.

The acoustic performance of the controller is quantified in terms of both sound pressure level and radiated sound power at the blade passage frequency. The measured sound pressure level reduction for the robust phase controller at microphone M1 is 11 dB at the blade passage frequency. The measured sound pressure level reduction for the aggressive phase controller at microphone M1 is 17 dB at the blade passage frequency. This reduction in sound pressure level at the blade passage frequency is consistent with the expected results and supports the claim that phase control could be used to modify the acoustic directivity of a vehicle. Further, the controller is demonstrated to reduce the radiated sound power of the vehicle at the blade passage frequency by 6 dB. Finally, the controller is shown to be capable of tracking small speed reference changes that are typical during flight, while still reducing the sound pressure level at the M1 microphone.

These results are demonstrated in the NASA Langley SALT anechoic chamber, where the only aerodynamic disturbance is caused by recirculation. In future work, a more realistic testing environment will be used that allows flight conditions of the propeller to be recreated. These conditions should include wind gusts and wind environments that are not perpendicular to the propeller plane.

In addition to these modifications to the testing environment, the controller, which is currently designed for steady-state performance, can be improved to dynamically track changes to phase and speed target changes. Phase changes are necessary for dynamically altering the directivity of the acoustic radiation pattern. Speed changes are expected to be required by the path planning and stabilizing controllers of the aircraft. A phase controller that has stability certificates for specific magnitudes of speed changes will define feasible speed changes generated by stabilizing and path planning controllers while still maintaining acceptable phase errors. In future work, a multirate $\mathcal{L}_1$ controller [12] will be tested for disturbance rejection. The multirate $\mathcal{L}_1$ controller is chosen to handle the multirate nature of the problem, where there are different control objectives operating at different timescales, e.g., aircraft stabilization and phase control.

Acknowledgments

This work is supported by the National Aeronautics and Space Administration (NASA). The authors would like to thank Dr. Kyle Pascioni of the NASA Langley Aeroacoustics Branch for his guidance on acoustic modelling.

References

[1] Johnston, J., and Donham, R., "Attenuation of Propeller-Related Vibration and Noise," *Journal of Aircraft*, 1981. doi: 10.2514/6.1981-521.

[2] Blunt, D., "Optimisation and Adaptive Control of Aircraft Propeller Synchrophase Angles," Ph.D. thesis, The University of Adelaide, 2012.

[3] Patterson, A., Gahlawat, A., and Hovakimyan, N., "Propeller Phase Synchronization for Small Distributed Electric Vehicles," *AIAA Intelligent Systems Conference*, 2019. doi:10.2514/6.2019-1458.

[4] Pascioni, K. A., and Rizzi, S., "Tonal Noise Prediction of a Distributed Propulsion Unmanned aerial Vehicle," *AIAA Aeroacoustics Conference*, 2018. doi:10.2514/6.2018-2951.

[5] Rothhaar, P., Murphy, P., Bacon, B., Gregory, I., Grauer, J., Busan, R., and Croom, M., "NASA Langley Distributed Propulsion VTOL Tilt-Wing Aircraft Testing, Modeling, Simulation, Control, and Flight Test Development," *AIAA Aviation Technology, Integration, and Operations Conference*, 2014. doi:10.2514/6.2014-2999.

[6] Fredericks, W., Moore, M., and Busan, R., "Benefits of Hybrid-Electric Propulsion to Achieve 4X Increase in Cruise Efficiency for a VTOL Aircraft," *AIAA Aviation Technology, Integration, and Operations Conference*, 2013. doi:10.2514/6.2013-4324.

[7] Stoll, A., Bevirt, J., Moore, M., Fredericks, W., and Borer, N., "Drag Reduction Through Distributed Electric Propulsion," *AIAA Aviation Technology, Integration, and Operations Conference*, 2014. doi:10.2514/6.2014-2851.

[8] Pascioni, K. A., Rizzi, S., and Aumann, A., "Auralization of an Unmanned aerial vehicle under propeller phase control," *Inter-Noise*, 2018.

[9] Pascioni, K. A., Rizzi, S. A., and Schiller, N., "Noise Reduction Potential of Phase Control for Distributed Propulsion Vehicles," *AIAA Aeroacoustics Conference*, 2019. doi:10.2514/6.2019-1069.

[10] Schiller, N., Pascioni, K., and Zawodny, N., "Tonal Noise Control using Rotor Phase Synchronization," *Vertical Flight Society Forum 75*, 2018.

[11] Shoemake, K., "Animating Rotation with Quaternion Curves," *ACM SIGRAPH Computer Graphics 19, no 3*, 1985. doi: 10.1145/325165.325242.

[12] Jafarnejadsani, H., Lee, H., and Hovakimyan, N., "$\mathcal{L}_1$ adaptive sampled-data control for uncertain multi-input multi-output systems," *Automatica*, 2019. doi:10.1016/j.automatica.2019.01.007.

VIII. Appendix

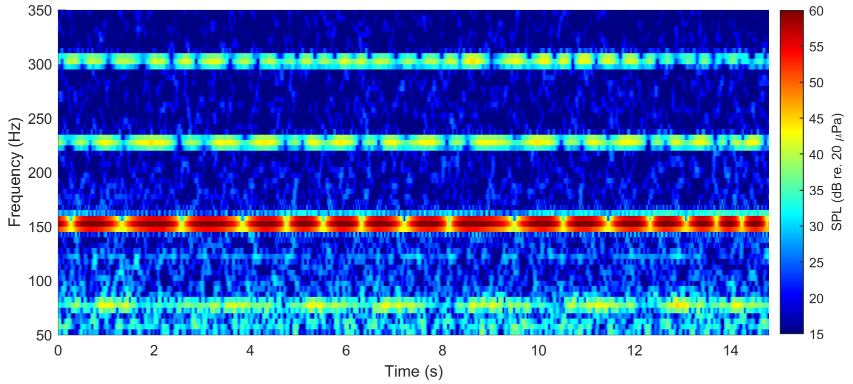

(a) Sound pressure level over time for uncontrolled phase.

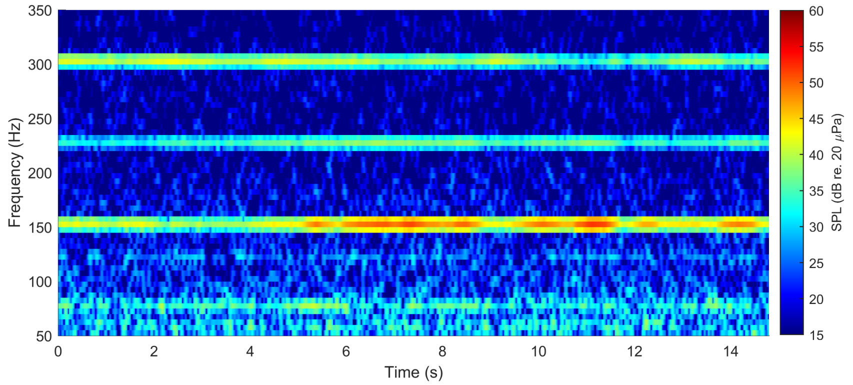

(b) Sound pressure level over time for robust phase controller.

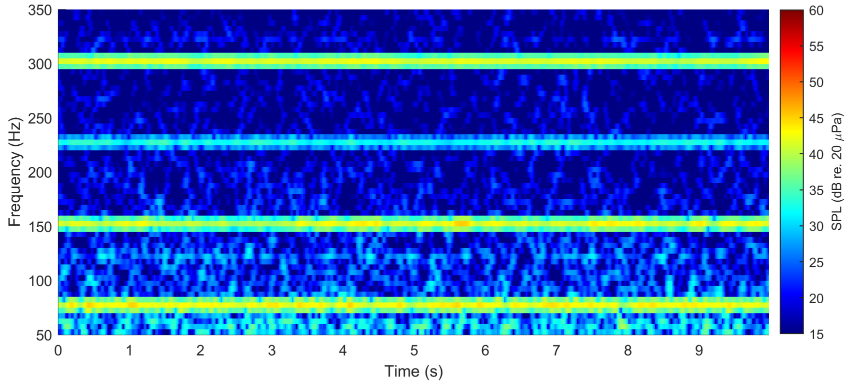

(c) Sound pressure level over time for aggressive phase controller.

Figure 9 Spectrograms for three phase control cases.